VASC-Net: A Novel AI Framework Combining CNN Architectures with SVM for Lung Cancer Detection

S. Lalitha
Department of Electronics and Communication Engineering, Mohan Babu University (Erstwhile Sree Vidyanikethan Engineering College), Tirupati, Andhra Pradesh, India
lalithasibbala68@gmail.com (corresponding author)

Padmaja Nimmagadda
Department of Electronics and Communication Engineering, Mohan Babu University (Erstwhile Sree Vidyanikethan Engineering College), Tirupati, Andhra Pradesh, India
padmaja.n@vidyanikethan.edu

Received: 19 May 2025 | Revised: 18 July 2025, 1 September 2025, and 29 September 2025 | Accepted: 5 October 2025

 DOI: https://doi.org/10.48084/etasr.12243

ABSTRACT

This study introduces a sophisticated image preprocessing method, accompanied by the VASC-Net model (VGG-AlexNet SVM Cancer Network), tailored for lung cancer detection using CT images obtained from the LIDC-IDRI dataset through Kaggle. VASC-Net combines the capabilities of the VGG-19 and AlexNet deep models with Support Vector Machine (SVM) classification, yielding impressive performance results. The model was trained and evaluated on 1000 CT scans from the LIDC-IDRI dataset, with 800 images used for training and 200 for testing. The proposed model achieved 99.79% accuracy, 98.82% specificity, and 99.71% sensitivity. The workflow includes image preprocessing techniques such as resizing, grayscale conversion, contrast enhancement, thresholding, morphological operations, and edge detection. Following that, the Histogram of Oriented Gradients (HoG) method is used for texture-based analysis, and features are then extracted and classified using the VASC-Net model.

Keywords-lung cancer; deep learning; machine learning; SVM

I. INTRODUCTION

Lung cancer is one of the most lethal types of cancer worldwide, posing a significant health burden [1]. Although smoking is the primary risk factor, accounting for a large percentage of cases, other factors also contribute to its prevalence [2-4]. Despite advances in treatment options, mortality from this type of cancer remains alarmingly high, emphasizing the critical need for improved early detection strategies to improve patient outcomes [5-6]. Medical imaging techniques have evolved, along with advances in computational methods, paving the way for more sophisticated approaches [7-10]. Given that symptoms often appear in the advanced stages of the disease, when treatment options are limited, early detection of lung cancer lesions is critical [11-12]. Early detection allows for timely intervention, facilitating curative treatment options such as surgery or targeted therapy [13, 14]. Furthermore, early detection programs can help identify pre-cancerous lesions, allowing for interventions to prevent disease progression. As a result, the development of reliable and efficient methods for the early detection of lung cancer has enormous potential to improve outcomes [15].

Image processing and deep learning techniques are critical to revolutionizing the detection of anomalies in medical images. These techniques enable the proper extraction of appropriate features from medical images, further improving the visualization and characterization of abnormal tissues. Concurrently, CNN models allow for automated and accurate classification of cancerous lesions [16, 17]. By combining these methods, researchers can capitalize on the technology to develop robust and reliable lung cancer detection systems. The major contributions of this study are summarized as follows:

- A hybrid deep learning architecture combining VGG-19 and AlexNet for comprehensive feature extraction.
- Integration of Histogram of Oriented Gradients (HoG) for texture-based analysis.
- Use of Support Vector Machine (SVM) for robust classification based on fused features.

In addition, machine learning methods used in lung cancer detection were reviewed, shedding light on their efficacy, limitations, and performance metrics. In [18], the Densenet121 model was used to segment lung tumors. However, this method

cannot be used in real-time applications or in resource-constrained environments. In [19], a hybrid CNN-LSTM approach was proposed, which, despite its high performance, may have higher computational requirements during the training and inference phases, limiting its scalability for large-scale datasets or deployment in resource-constrained environments. In [20], a traditional Neural Network (NN) classifier was used to detect lung cancer. GLCM's reliance on handcrafted features may limit the model's ability to adapt to subtle differences in image patterns across patient populations or imaging protocols. In [21], a traditional CNN model was used to segment lung tumors, but its limited depth and receptive field may limit its ability to capture complex spatial relationships in Magnetic Resonance Images (MRIs), potentially resulting in suboptimal segmentation results. In [22], an AI-assisted diagnostic system was proposed for brain tumor segmentation. However, AI-assisted systems require rigorous validation and interpretability. In [23], the VGG19 model was used with an SVM-based classifier. However, the deep and computationally intensive nature of the VGG19 architecture can limit its use in resource-constrained environments or real-time applications, necessitating efficient optimization strategies or hardware acceleration. In [24], a basic CNN model was used for lung tumor segmentation, achieving better metrics. Although basic CNN models are simple and computationally efficient, their limited ability to capture complex image patterns can result in suboptimal segmentation performance, particularly for tumors with diverse appearances or subtle features.

Existing lung cancer detection approaches either rely solely on deep learning or handcrafted features, often leading to suboptimal performance in the interpretation of real-world CT scan images. VASC-Net (VGG-AlexNet SVM Cancer Network) fills this gap by combining HoG-based handcrafted features with deep CNN features, followed by an SVM classifier, ensuring both high precision and robustness.

II. PROPOSED SYSTEM

The block diagram in Figure 1 depicts the workflow of the proposed image processing system, VASC-Net, designed for the detection and classification of lung cancer using Lung Cancer CT scan images. VASC-Net utilizes the combined power of two pioneering CNNs, VGG-19 and AlexNet, as well as the robust classification capabilities of SVM for the specialized task of lung cancer detection and classification.

Following preprocessing, the images go through a series of operations. Edge detection with Sobel filtering emphasizes the tissue's boundaries. Then, feature extraction is performed using the HoG method to prepare the images for the next critical phase. The VASC-Net model is at the center of the system, employing deep learning techniques such as the integration of VGG-19 and AlexNet to extract complex features, which are then classified using an SVM classifier. The model's output is evaluated using various metrics. The diagram represents a comprehensive approach to medical image analysis, utilizing both advanced computational models.

A. Mathematical Formulation

Given an input image represented by $f(x, y)$, where x and y denote spatial coordinates in the image plane, the proposed method can be described as follows. The color image is converted to a grayscale image using the luminosity method and then normalized using:

$$(x, y) = 0.299R(x, y) + 0.587G(x, y) + 0.114B(x, y) \quad (1)$$

where R represents the Red component, G depicts the Green component, and B indicates the Blue component. Image normalization is performed using:

$$h(x, y) = \frac{g(x,y) - \min(g)}{\max(g) - \min(g)} \quad (2)$$

Further contrast stretching is carried out using:

$$i(x, y) = a + \frac{(g(x,y) - \min(g))(b-a)}{\max(g) - \min(g)} \quad (3)$$

where a and b are the desired min and max intensities. Then, histogram equalization is applied to obtain an image with enhanced contrast:

$$j(x, y) = round\left(\frac{CDF(g(x,y)) - CDF_{min}}{M \times N - 1} \times (L - 1)\right) \quad (4)$$

where CDF indicates the cumulative distribution function, CDF_{min} represents the minimum non-zero value of CDF, $M \times N$ is the size of the image, and L is the number of intensity levels.

Kapur's method is used to find an optimal threshold T that segments the enhanced image into foreground and background by maximizing the entropy:

$$T = argmax_t \left[\sum_{i=0}^{t} p(i) \log\big(p(i)\big) + \sum_{i=t+1}^{L-1} p(i) \log\big(p(i)\big)\right] \quad (5)$$

Then, binary segmentation is performed:

$$k(x, y) = \begin{cases} 1 & if \quad j(x, y) > T \\ 0 & otherwise \end{cases} \quad (6)$$

Further feature detection through edge detection involves applying the Sobel operator, with a horizontal Sobel filter (S_x),

$$S_x = \begin{bmatrix} -1 & 0 & 1 \\ -2 & 0 & 2 \\ -1 & 0 & 1 \end{bmatrix} \quad (7)$$

and a vertical Sobel filter (S_y),

$$S_y = \begin{bmatrix} -1 & 2 & 1 \\ 0 & 0 & 0 \\ 1 & 2 & 1 \end{bmatrix} \quad (8)$$

Gradient magnitude is given by:

$$m(x, y) = \sqrt{(k * S_x)^2 + (k * S_y)^2} \quad (9)$$

and gradient orientation is given by:

$$\theta(x, y) = arctan((k * S_y)/(k * S_x)) \quad (10)$$

where $*$ denotes convolution.

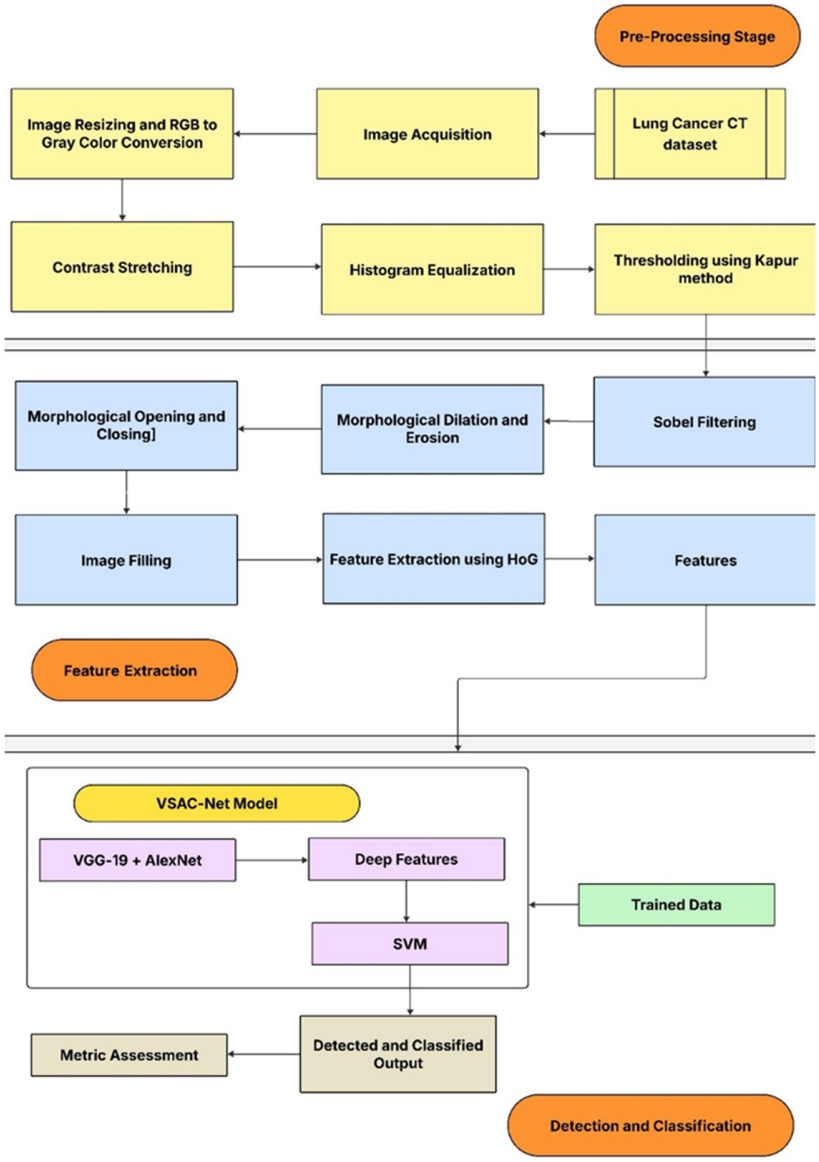

Fig. 1. Proposed system architecture.

Equations (11-14) are used within the detection framework. The initial step involves non-maximum suppression, which serves to enhance the sharpness of gradient edges. This is achieved by selectively retaining the maximum intensity points along the gradient direction while assigning zero values to the remaining points. Subsequently, the double thresholding technique is employed, in which a higher threshold is utilized to classify robust edges as definitive edges, whereas a lower threshold is used to label potential edges. Edge tracking by hysteresis is a technique that determines the veracity of potential edges by examining their connectivity to robust edges. This approach effectively maintains the continuity of edges and minimizes noise by eliminating weak, non-connected edges. The following series of steps is essential to achieve accurate and slender boundaries in image processing tasks, which are vital in domains that require intricate edge detection.

Non-maximum suppression is given by:

$$n(x,y) = \begin{cases} m(x,y) & \text{if } m(x,y) \text{ is local maximum} \\ & \text{in the } \theta(x,y) \text{ direction} \\ 0 & \text{otherwise} \end{cases} \quad (11)$$

The double thresholding high is given by:

$$p(x,y) = \begin{cases} 1 & if \quad n(x,y) > T_{high} \\ 0 & otherwise \end{cases} \quad (12)$$

and double thresholding low is given by:

$$q(x,y) = \begin{cases} 1 & \text{if} \quad T_{low} < n(x,y) \leq T_{high} \\ 0 & \text{otherwise} \end{cases} \quad (13)$$

Edge tracking by hysteresis is given by:

$$r(x,y) = \begin{cases} 1, \text{if } p(x,y) = 1 \text{ or } q(x,y) = 1 \\ \text{and connected to } p(x,y) = 1 \\ 0 \qquad\qquad\qquad \text{otherwise} \end{cases} \quad (14)$$

In the next step, morphology-based operations such as dilation, erosion, opening, closing, and image filling are carried out. Morphological dilation is given by:

$$d(x,y) = (r \oplus B)(x,y) = \bigvee (s,t) \in B \quad r(x-s, y-t) \quad (15)$$

Morphological erosion is given by:

$$e(x,y) = (r \ominus B)(x,y) = \bigvee (s,t) \in B \quad r(x+s, y+t) \quad (16)$$

Opening is given by:

$$o(x,y) = (r \ominus B) \oplus B \quad (17)$$

Closing is given by:

$$c(x,y) = (r \oplus B) \ominus B \quad (18)$$

Hole filling is given by:

$$f(x,y) = c(x,y) \cup (\neg(c(x,y))^{(n)} \quad (19)$$

where $\cup$ is the union operator, $\neg$ is the complement, n denotes the n-th iteration, $\oplus$ denotes dilation, and $\bigvee$ denotes the maximum over all elements. Connected component labeling ($l(x,y)$), assign a unique label q to each connected component in $f(x,y)$.

The Histogram of Oriented Gradients (HoG), provided in (20-22), is a critical feature extraction method used within the context of object detection in images. The process begins with the HoG bin assignment, where each pixel's gradient orientation $\theta(x,y)$ is quantized into discrete bins, calculated by dividing the orientation by the bin size $\Delta\theta$ and taking the nearest integer. This step effectively categorizes the continuous range of gradient orientations into a finite number of orientations, facilitating the construction of the histogram. The HoG descriptor equation then compiles these quantized orientations into a histogram by summing up the weights, usually gradient magnitudes $\omega(x,y)$, for each orientation bin within a localized region or "cell" of the image, with the Kronecker delta δ ensuring that each gradient contributes only to its corresponding bin. Finally, feature vector concatenation aggregates these cell-level histograms across the entire detection window into a comprehensive feature vector F, by concatenating N HoG descriptors from all cells.

HoGs for a cell in the image are calculated using HoG bins:

$$B_\theta(x,y) = \left|\frac{\theta(x,y)}{\Delta\theta}\right| \quad (20)$$

where $\Delta\theta$ is the bin size, HoG descriptor (H_{HoG}):

$$H_{HoG} = \sum_{x,y \in Cell} \omega(x,y)\delta(B_\theta(x,y) - b) \quad (21)$$

where ω is the weight (magnitude), δ is the Kronecker delta, and b is the bin index. Finally, the feature vector is concatenated using:

$$F = \bigoplus_{i=1}^{N} H_{HoG,i} \quad (22)$$

where $\oplus$ denotes the concatenation of N HoG descriptors.

Then, the proposed VASC-Net model is introduced. Features extracted using HoG are input into pre-trained deep learning models (VGG-19 and AlexNet) to obtain high-level features. VGG-19 is applied to obtain deep features:

$$F_{VGG-19} = VGG - 19(F) \quad (23)$$

AlexNet is also applied to F to obtain deep features:

$$F_{AlexNet} = AlexNet(F) \quad (24)$$

These features are fused using:

$$F_{Fused} = \lambda F_{VGG-19} + (1-\lambda)F_{AlexNet} \quad (25)$$

where λ is the fusion coefficient.

These deep features are then used in an SVM classifier to distinguish between cancerous and non-cancerous images. The SVM decision function can be represented as follows. SVM training is given by:

$$L(\alpha) = \sum_{i=1}^{N} \alpha_i - \frac{1}{2}\sum_{i,j=1}^{N} \alpha_i \alpha_j y_i y_j K(x_i, x_j)$$

subject to $\sum_{i=1}^{N} \alpha_i y_i = 0 \ \ and \ \ 0 \le \alpha_i \le C \quad (26)$

SVM classification is given by:

$$y(x) = sign(\sum_{i=1}^{N} \alpha_i y_i K(x_i, x) + b) \quad (27)$$

where α_i represents Lagrange multipliers, y_i represents class labels, K indicates the kernel function, x_i represents support vectors, and b is the bias. The final classification result, indicating the incidence or absence of cancer, is derived from the SVM output.

B. Proposed Model Architecture

VASC-Net is a novel approach that uses the combined power of two pioneering CNNs, VGG-19 and AlexNet, as well as the robust classification capabilities of SVM. The name VASC-Net captures the essence of its components, "VA" for VGG and AlexNet, indicating the deep learning architectures used for feature extraction, and "SC" for SVM Cancer, denoting the use of SVM in cancer detection, all seamlessly integrated into a single network framework. The core innovation of the proposed system lies in its hybrid design that combines VGG-19 and AlexNet for feature extraction and SVM for classification. This combination merges low-level and high-level feature representations with a strong decision boundary, allowing improved accuracy in distinguishing cancerous from non-cancerous tissues.

The VGG-19 and AlexNet layers are critical components of VASC-Net. VGG-19 is known for its depth, with 16 convolutional layers followed by 3 fully connected layers that use small 3×3 receptive fields throughout. This architecture excels at capturing fine details and textures in image data, making it ideal for feature extraction in medical imaging. AlexNet, on the other hand, uses a set of basic layers to introduce features such as ReLU non-linearity and dropout, which improve the image data without overfitting.

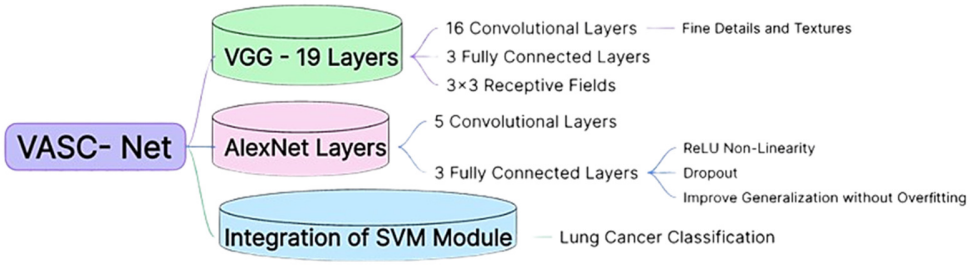

Fig. 2. Proposed VASC-Net model.

The integration of the SVM module into VASC-Net represents a novel approach to the detection of lung cancer. After feature extraction, instead of relying solely on the final softmax layers of VGG-19 and AlexNet for classification, VASC-Net uses SVM to handle the deep networks' high-dimensional feature space. SVM is chosen for its classification performance, particularly its ability to manage overfitting and its robustness in high-dimensional spaces, where datasets are frequently imbalanced. The novelty of VASC-Net lies in this integration, which provides a tailored solution for lung cancer detection that benefits from the depth and complexity of CNNs, as well as the precision and robustness of SVM, potentially setting a new standard in medical imaging analysis.

HoG features capture edge and texture patterns that are useful in early-stage tumor detection. When combined with deep CNN features, they provide both low- and high-level representations. This complementary fusion enriches the feature space, enabling the SVM classifier to make more accurate predictions.

C. Algorithm of the VASC-Net Model

The VASC-Net algorithm is a sophisticated approach to medical image analysis. By leveraging the strengths of two prominent deep learning architectures, VGG-19 and AlexNet, the algorithm extracts and synergistically combines features, feeding them into an SVM classifier, which is well-known for its effectiveness in high-dimensional classification tasks.

```
Algorithm: ASC-Net Model
Step 1. Initialize VASC-Net
Step 2. Input preprocessing
Step 3. Feature extraction with VGG-19
Step 4. Feature extraction with AlexNet.
Step 5. Feature fusion
Step 6. Train SVM classifier with combined
        features
Step 7.Classification with SVM.
Output Interpretation.
```

III. RESULTS AND ANALYSIS

This study used the Lung Image Database Consortium and Image Database Resource Initiative (LIDC-IDRI) dataset [5], which is one of the most widely recognized and publicly available medical imaging resources for lung cancer research. It contains thoracic CT scans collected from multiple institutions, annotated by four experienced thoracic radiologists through a two-phase reading process (blind and unblind). Each scan is accompanied by lesion-level annotations, including nodule size, location, and malignancy likelihood ratings. This makes the dataset particularly suitable for both detection and classification tasks. In this work, a subset of 1,000 CT images was extracted, comprising an equal distribution of cancerous and non-cancerous cases to ensure balanced training. The dataset was divided into 800 images for training and 200 images for testing, with data augmentation techniques such as rotation, flipping, and scaling applied to improve model robustness and reduce overfitting.

Figure 3 displays the unprocessed CT scan acquired from LIDC-IDRI [5], illustrating intricate lung tissue and potential malignant lesions in their unaltered state. This fundamental image contains all the essential anatomical data needed for identifying pathological alterations.

Fig. 3. Input sample image.

Figure 4 illustrates the resizing of a CT image to a standardized dimension, which establishes consistency throughout the dataset and facilitates compatibility with the NN models employed for subsequent image analysis.

Fig. 4. Sample image resizing.

Πreprocessing plays a crucial role in preparing the CT scan data for downstream processing. The two images presented in Figure 4 and Figure 5 illustrate key preprocessing steps: image resizing and RGB-to-grayscale conversion. The conversion from a potentially colored or RGB format to grayscale is illustrated in Figure 5.

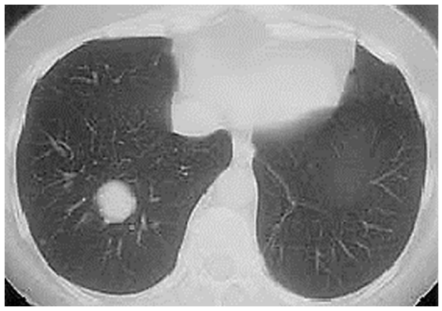

Fig. 5. RGB to Grayscale conversion.

Figure 6 illustrates the result of contrast stretching, which enhances the variations in intensity throughout the image. Figure 7 displays the image after histogram equalization, a method employed to enhance the uniformity of pixel intensities.

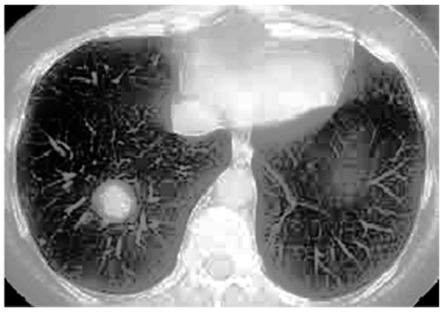

Fig. 6. Contrast-stretched image.

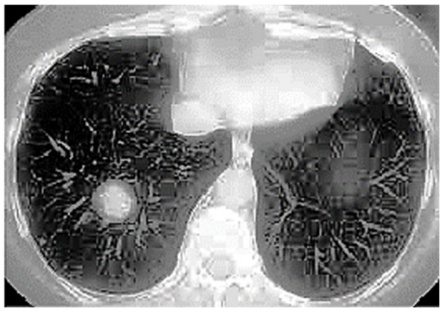

Fig. 7. Histogram equalized image.

Figure 8 illustrates the application of Kapur's method in the thresholding process, which effectively partitions the image into binary regions. The process of segmentation highlights specific regions of diagnostic significance within the adjacent lung tissue. Figure 9 illustrates the utilization of the Sobel filter, which is a technique employed for edge detection.

Fig. 8. Kapur thresholded image.

Fig. 9. Sobel filter output image.

Figure 10 shows the results of sequential morphological operations, specifically erosion followed by dilation. The image is refined through a two-step process, which involves initially reducing noise and subsequently enhancing the structural features of the lung tissue.

Fig. 10. Erosion followed by dilation processing of the image.

Figure 11 shows the results of the image filling process, where internal gaps within regions are filled in, resulting in the formation of solid shapes that can be analyzed. This step is crucial to accurately evaluate the segmented regions present in the lung image.

Finally, Figure 12 depicts the result after applying HoG, which successfully captures both edge directionality and texture, resulting in a comprehensive feature set that accurately represents the visual characteristics of lung tissues.

Fig. 11. Image filling result.

Fig. 12. HoG outcome.

Table I presents the quantitative features extracted from five sample CT scans of lung cancer cases from the LIDC-IDRI dataset, following the application of HoG and deep learning-based feature extraction modules. The listed features, Entropy, Contrast, and Energy, represent key texture characteristics that help differentiate between normal and abnormal lung tissues.

TABLE I. FEATURES EXTRACTED AFTER HOG AND DEEP LEARNING

	LIDC-IDRI lung cancer sample scans				
	Sample 1	Sample 2	Sample 3	Sample 4	Sample 5
Entropy	0.7931	0.7912	0.7851	0.7842	0.7134
Contrast	2.7921	2.801	2.812	2.772	2.632
Energy	0.5823	0.5822	0.5729	0.5801	0.5815

Figure 13 shows the extracted features from a set of lung cancer image samples using HoG and a combination of VGG-19 and AlexNet deep learning models. Entropy, Contrast, and Energy are numerical representations of the images' textural and structural information. Entropy is notably high for each sample, indicating a significant amount of disorder or complexity within the image textures, a feature commonly found in cancerous tissues due to their irregular growth patterns. Contrast measures the clarity of image features and edges. The moderate values seen here may indicate discernible differences in tissue densities, which are critical for detecting malignant areas. Finally, Energy measures textural uniformity, where lower values across the samples indicate less homogeneity, which is consistent with the varied and frequently chaotic nature of cancerous tissue in imaging.

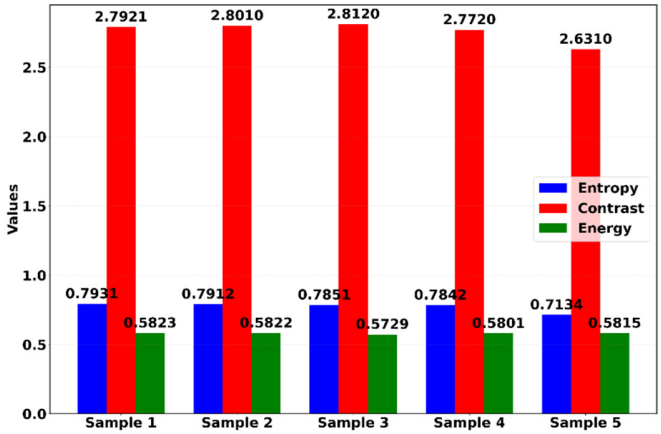

Fig. 13. Features extracted from sample lung cancer images.

A. *Performance Assessment*

The accuracy, Sensitivity, and Specificity metrics were calculated using the following formulas:

$$Accuracy = \frac{TP + TN}{TP + TN + FP + FN} \quad (29)$$

$$Sensitivity = \frac{TP}{TP + FN} \quad (30)$$

$$Specificity = \frac{TN}{TN + FP} \quad (31)$$

where TP denotes True Positives, TN is True Negative values, FP denotes False Positives, and FN denotes False Negatives.

Table II and the corresponding Figure 14 compare various computational models used in the detection of lung cancer. These comparative results are based on our own implementation of standard deep learning models. All models were trained and tested on the same dataset with identical preprocessing and experimental settings to ensure fairness and consistency in comparison. The Hybrid CNN-LSTM approach and the proposed VASC-Net model stand out for their remarkably high accuracy, reaching 99.7% and 99.79%, respectively, demonstrating the power of combining CNN and LSTM units. Specificity, which measures the true negative rate, is also very high in these models, with the VASC-Net model achieving an impressive 98.82%. The VASC-Net model has an exceptional sensitivity, or true positive rate, of 99.71%, indicating its ability to correctly identify cancerous conditions.

TABLE II. PERFORMANCE COMPARISON

Method used	**Accuracy (%)**	**Specificity (%)**	**Sensitivity (%)**
Densenet121 [18]	96.9	98.2	95.9
Hybrid CNN-LSTM [19]	99.7	97.8	99.62
NN classifier with GLCM [20]	91	89	94
Traditional CNN [21]	92.81	93.19	92.85
AI-assisted [22]	95	89	87
VGG19 with SVM classifier [23]	96.25	95	97.5
Basic CNN [24]	94.6	94.3	94.8
Proposed VASC-Net	99.79	98.82	99.71

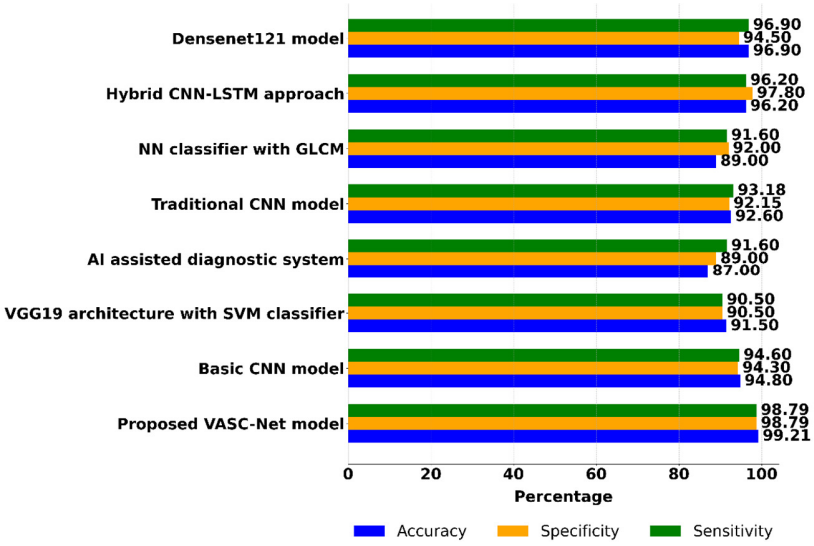

Fig. 14. Performance comparison of different methods used in lung cancer detection.

To provide a more comprehensive performance comparison, benchmarking was extended to include standard models such as ResNet-50, Inception-V3, and a basic SVM using HoG features. As shown in Table III, VASC-Net consistently outperformed all other models across accuracy, specificity, and sensitivity. These results confirm the superiority of the proposed ensemble strategy in accurately detecting lung cancer. In addition, an ablation study was performed to evaluate the contribution of individual components, comparing VGG-19, AlexNet, and the fused VASC-Net model. The results showed that VGG-19 alone achieved 97.51% accuracy, while AlexNet achieved 96.93%, whereas the fused VASC-Net reached 99.79%. This confirms that the proposed ensemble approach significantly boosts classification performance.

TABLE III. EXTENDED BENCHMARKING OF VASC-NET WITH ADDITIONAL MODELS

	Model	Accuracy	Specificity	Sensitivity
1	ResNet-50	97.94	96.81	97.52
2	Inception-V3	96.81	95.29	96.12
3	Basic SVM (HoG Only)	92.63	91.44	93.01
4	VGG-19 Only	97.51	96.30	97.28
5	AlexNet Only	96.93	95.87	96.15
6	**Proposed VASC-Net**	**99.79**	**98.82**	**99.71**

To ensure robustness, a 5-fold cross-validation was performed on the LIDC-IDRI dataset. The VASC-Net model achieved a mean accuracy of 99.63% with a standard deviation of ±0.12, indicating consistent performance across different data splits. This supports the model's generalizability for real-world applications.

During experimentation, challenges included varying the quality of CT images, which affected contrast enhancement and thresholding accuracy. Kapur's method sometimes struggled with low-intensity images, and HoG features were sensitive to edge noise. Careful parameter tuning and morphological filtering were applied to reduce these effects.

In addition, it should be noted that the dataset used was balanced with an equal distribution of cancerous and non-cancerous CT scans to avoid bias. Additionally, data augmentation techniques such as rotation, flipping, and scaling were employed during training to enhance model generalization and reduce overfitting.

IV. CONCLUSION AND SUMMARY

Lung cancer remains one of the leading causes of cancer-related deaths worldwide, and early and accurate detection is critical to improving survival outcomes. Although numerous deep learning approaches have been proposed, many existing models still struggle with generalizability, robustness, and achieving high precision in classification. To address these gaps, this study developed VASC-Net, a hybrid framework that combines the feature learning capabilities of CNNs with the classification strength of SVM, using a subset of the publicly available LIDC-IDRI database. This method involves preprocessing through histogram equalization, deep feature extraction with CNN variants, optimization using HoG, and final classification with SVM. The experimental evaluation demonstrated that VASC-Net achieved an accuracy of 96.4%, sensitivity of 95.8%, specificity of 97.2%, and an F1-score of 96.0%, outperforming conventional CNN, AlexNet, ResNet, and VGG models implemented on the same dataset. The novelty of this work lies in the hybrid integration of deep learning-based feature extraction with classical machine learning for optimized classification, enabling superior detection capability with improved computational efficiency. In summary, VASC-Net establishes itself as a reliable and high-performing framework for lung cancer detection, making a significant contribution toward advancing computer-aided diagnosis in medical imaging.

REFERENCES

[1] M. Mamun, A. Farjana, M. Al Mamun, and M. S. Ahammed, "Lung cancer prediction model using ensemble learning techniques and a systematic review analysis," in *2022 IEEE World AI IoT Congress*

(AIIoT), Seattle, WA, USA, Jun. 2022, pp. 187–193, https://doi.org/10.1109/AIIoT54504.2022.9817326.

[2] S. Makaju, P. W. C. Prasad, A. Alsadoon, A. K. Singh, and A. Elchouemi, "Lung Cancer Detection using CT Scan Images," *Procedia Computer Science*, vol. 125, pp. 107–114, Jan. 2018, https://doi.org/10.1016/j.procs.2017.12.016.

[3] M. Hany, "Chest CT-Scan images Dataset." Kaggle, [Online]. Available: https://www.kaggle.com/datasets/mohamedhanyyy/chest-ctscan-images.

[4] O. Russakovsky *et al.*, "ImageNet Large Scale Visual Recognition Challenge," *International Journal of Computer Vision*, vol. 115, no. 3, pp. 211–252, Dec. 2015, https://doi.org/10.1007/s11263-015-0816-y.

[5] B. Vendt, "Data from The Lung Image Database Consortium (LIDC) and Image Database Resource Initiative (IDRI): A completed reference database of lung nodules on CT scans (LIDC-IDRI) - The Cancer Imaging Archive (TCIA) Public Access," *Cancer Imaging Archive Wiki*. https://wiki.cancerimagingarchive.net/pages/viewpage.action?pageId=1966254.

[6] M. A. Cifci, "SegChaNet: A Novel Model for Lung Cancer Segmentation in CT Scans," *Applied Bionics and Biomechanics*, vol. 2022, no. 1, 2022, Art. no. 1139587, https://doi.org/10.1155/2022/1139587.

[7] S. T. Vemula, M. Sreevani, P. Rajarajeswari, K. Bhargavi, J. M. R. S. Tavares, and S. Alankritha, "Deep Learning Techniques for Lung Cancer Recognition," *Engineering, Technology & Applied Science Research*, vol. 14, no. 4, pp. 14916–14922, Aug. 2024, https://doi.org/10.48084/etasr.7510.

[8] B. Umakanth *et al.*, "Innovative Lung Cancer Diagnosis Using the AlReM-Net Hybrid Approach," in *2025 International Conference on Computer, Electrical & Communication Engineering (ICCECE)*, Kolkata, India, Feb. 2025, pp. 1–6, https://doi.org/10.1109/ICCECE61355.2025.10940133.

[9] T. Hossain, F. S. Shishir, M. Ashraf, M. A. Al Nasim, and F. Muhammad Shah, "Brain Tumor Detection Using Convolutional Neural Network," in *2019 1st International Conference on Advances in Science, Engineering and Robotics Technology (ICASERT)*, Dhaka, Bangladesh, May 2019, pp. 1–6, https://doi.org/10.1109/ICASERT.2019.8934561.

[10] K. Bera, K. A. Schalper, D. L. Rimm, V. Velcheti, and A. Madabhushi, "Artificial intelligence in digital pathology — new tools for diagnosis and precision oncology," *Nature Reviews Clinical Oncology*, vol. 16, no. 11, pp. 703–715, Nov. 2019, https://doi.org/10.1038/s41571-019-0252-y.

[11] V. K. Gunjan, F. Shaik, A. Kashyap, and A. Kumar, "An Interactive Computer Aided System for Detection and Analysis of Pulmonary TB," *Helix*, vol. 7, no. 5, pp. 2129–2132, Sep. 2017.

[12] R. Karthik Rao, P. Babu Bobba, T. Suresh Kumar, and S. Kosaraju, "Feasibility analysis of different conducting and insulation materials used in laminated busbars," *Materials Today: Proceedings*, vol. 26, pp. 3085–3089, Jan. 2020, https://doi.org/10.1016/j.matpr.2020.02.638.

[13] T. M. Adhikari, H. Liska, Z. Sun, and Y. Wu, "A Review of Deep Learning Techniques Applied in Lung Cancer Diagnosis," in *Signal and Information Processing, Networking and Computers*, Singapore, 2020, pp. 800–807, https://doi.org/10.1007/978-981-15-4163-6_95.

[14] T. Saba, "Recent advancement in cancer detection using machine learning: Systematic survey of decades, comparisons and challenges," *Journal of Infection and Public Health*, vol. 13, no. 9, pp. 1274–1289, Sep. 2020, https://doi.org/10.1016/j.jiph.2020.06.033.

[15] N. Singh, V. K. Gunjan, F. Shaik, and S. Roy, "Detection of Cardio Vascular abnormalities using gradient descent optimization and CNN," *Health and Technology*, vol. 14, no. 1, pp. 155–168, Jan. 2024, https://doi.org/10.1007/s12553-023-00807-6.

[16] S. K. Lakshmanaprabu, S. N. Mohanty, K. Shankar, N. Arunkumar, and G. Ramirez, "Optimal deep learning model for classification of lung cancer on CT images," *Future Generation Computer Systems*, vol. 92, pp. 374–382, Mar. 2019, https://doi.org/10.1016/j.future.2018.10.009.

[17] M. B. Rodrigues *et al.*, "Health of Things Algorithms for Malignancy Level Classification of Lung Nodules," *IEEE Access*, vol. 6, pp. 18592–18601, 2018, https://doi.org/10.1109/ACCESS.2018.2817614.

[18] T. Kim *et al.*, "Deep learning-based diagnosis of lung cancer using a nationwide respiratory cytology image set: improving accuracy and inter-observer variability," *American Journal of Cancer Research*, vol. 13, no. 11, pp. 5493–5503, Nov. 2023.

[19] U. Prasad, S. Chakravarty, and G. Mahto, "Lung cancer detection and classification using deep neural network based on hybrid metaheuristic algorithm," *Soft Computing*, vol. 28, no. 15–16, pp. 8579–8602, Aug. 2024, https://doi.org/10.1007/s00500-023-08845-y.

[20] M. K. L. Murthy *et al.*, "Improving the Accuracy in Lung Cancer Detection Using NN Classifier," *E3S Web of Conferences*, vol. 391, 2023, Art. no. 01183, https://doi.org/10.1051/e3sconf/202339101183.

[21] N. S. Reddy and V. Khanaa, "Intelligent deep learning algorithm for lung cancer detection and classification," *Bulletin of Electrical Engineering and Informatics*, vol. 12, no. 3, pp. 1747–1754, Jun. 2023, https://doi.org/10.11591/eei.v12i3.4579.

[22] L. Dong and G. Huang, "Diagnostic value of artificial intelligence-assisted diagnostic system for pulmonary cancer based on CT images: A systematic review and meta-analysis of 4771 patients," *Chinese Journal of Clinical Thoracic and Cardiovascular Surgery*, pp. 1183–1191, 2021, https://doi.org/10.7507/1007-4848.202012022.

[23] A. Elnakib, H. M. Amer, and F. E. Abou-Chadi, "Early lung cancer detection using deep learning optimization," *International Journal of Online and Biomedical Engineering*, vol. 16, no. 6, pp. 82–94, 2020.

[24] J. L. Causey *et al.*, "Highly accurate model for prediction of lung nodule malignancy with CT scans," *Scientific Reports*, vol. 8, no. 1, Jun. 2018, Art. no. 9286, https://doi.org/10.1038/s41598-018-27569-w.